STRUCTURAL BIOLOGY

Conformational landscape alternations promote oncogenic activities of Ras-related C3 botulinum toxin substrate 1 as revealed by NMR

Yuki Toyama[1,2], Kenji Kontani[3], Toshiaki Katada[4], Ichio Shimada[1]*

Ras-related C3 botulinum toxin substrate 1 (Rac1) plays critical roles in the maintenance of cell morphology by cycling between inactive guanosine diphosphate (GDP)–bound and active guanosine triphosphate (GTP)–bound states. Rac1 P29S mutant is known to strongly promote oncogenesis by facilitating its intrinsic GDP dissociation and thereby increasing the level of the GTP-bound state. Here, we used solution nuclear magnetic resonance spectroscopy to investigate the activation mechanism of the oncogenic P29S mutant. We demonstrate that the conformational landscape is markedly altered in the mutant, and the preexisting equilibrium is shifted toward the conformation with reduced affinity for Mg^{2+}, a cofactor that is critical for maintaining stable GDP binding. Our results suggest that the alternation of the preexisting conformational equilibrium of proteins is one of the fundamental mechanisms underlying their oncogenic activities.

INTRODUCTION

Small guanine nucleotide–binding proteins (G proteins), also known as small guanosine triphosphatases (GTPases), are a large family of enzymes that function as binary molecular switches in the regulation of a wide variety of cellular activities (*1*). The small G proteins cycle between two distinct functional states: an inactive guanosine diphosphate (GDP)–bound state and an active guanosine triphosphate (GTP)–bound state. The aberrant functions of the small G proteins are closely related to pathological processes, such as oncogenesis. For example, oncogenic mutations of the Ras family of small G proteins are frequently found in a variety of human tumors (*2*).

Ras-related C3 botulinum toxin substrate 1 (Rac1) is a member of the Rho family of small G proteins. Rac1 plays critical roles in the maintenance of cell morphology and in cell migration. Recently, extensive sequencing analyses of human cancer cells have revealed that gain-of-function mutations of Rac1 are found in sun-exposed melanomas, human sarcoma cell lines, and breast cancer cell lines, and Rac1 has been identified as an essential growth driver that strongly promotes cell proliferations and the subsequent oncogenic activities (*3*–*5*). Therefore, Rac1 is considered to be a potential therapeutic target for cancer treatment (*6*). The Pro^{29}-to-Ser mutation, frequently found in melanoma, is located adjacent to the region called switch1 and is distinct from the hotspots (Gly^{12}, Gly^{13}, and Gln^{61}) found in oncogenic mutants of the Ras family (*2*, *7*, *8*). Biochemical studies of the P29S mutant have revealed that the mutant exhibits a "fast-cycling" property, in which GDP dissociation from the inactive GDP-bound state is accelerated, thereby increasing the level of the active GTP-bound state (*5*, *9*). Despite its biological importance, the elucidation of the molecular mechanism underlying the fast-cycling behavior has been impeded by the lack of detailed structural information about the inactive GDP-bound state of Rac1 and its mutants. Here, we used solution nuclear magnetic resonance (NMR) spectroscopy, which can characterize the dynamic nature of proteins at atomic resolution, to determine the activation mechanism of the Rac1 P29S oncogenic mutant.

[1]Graduate School of Pharmaceutical Sciences, The University of Tokyo, Hongo, Bunkyo-ku, Tokyo 113-0033, Japan. [2]Japan Biological Informatics Consortium (JBiC), Aomi, Koto-ku, Tokyo 135-0064, Japan. [3]Department of Biochemistry, Meiji Pharmaceutical University, Kiyose, Tokyo 204-8588, Japan. [4]Molecular Cell Biology Laboratory, Research Institute of Pharmaceutical Sciences, Faculty of Pharmacy, Musashino University, Tokyo 202-8585, Japan.
*Corresponding author. Email: shimada@iw-nmr.f.u-tokyo.ac.jp

RESULTS

Reduced affinity for Mg^{2+} in the P29S mutant

Pro^{29} is located adjacent to the switch1 region (residues 30 to 38), which stabilizes the bound GDP through the interaction with the bound Mg^{2+} coordinated to the carbonyl oxygen of Thr^{35} (Fig. 1A) (*8*). In the case of Rac1, the bound Mg^{2+} stabilizes the GDP binding, and the removal of Mg^{2+} markedly increases the GDP dissociation rate by about 300-fold (*10*). Therefore, we focused on the effects of the P29S mutation on the Mg^{2+} binding to investigate the mechanism underlying the accelerated GDP dissociation. We found that the dissociation rate of GDP increases as the concentration of Mg^{2+} decreases, consistent with the previous report (*10*), and estimated the apparent dissociation constant (K_d) of Mg^{2+} to be 8.9 ± 0.7 μM in the wild type (Fig. 1, B and C, and table S1). In the P29S mutant, we found that the inherent GDP dissociation rate in the absence of Mg^{2+} was only 2.6-fold faster than that of the wild type, whereas the ratio increased up to 8-fold under the physiological Mg^{2+} conditions in the submillimolar range (*11*). This is because the apparent K_d of Mg^{2+} in the P29S mutant (25.8 ± 2.3 μM) is about threefold weaker than that of the wild type, and the population of the Mg^{2+}-unbound state is increased in the P29S mutant (Fig. 1, B and C, and table S1). Because the GDP dissociation is greatly accelerated in the Mg^{2+}-unbound state, this relatively small increase in the Mg^{2+}-unbound population substantially affects the overall GDP dissociation rate. These results revealed that the accelerated GDP dissociation in the P29S mutant is mainly attributed to its reduced affinity for Mg^{2+}.

To investigate the structural mechanism for the differences in the Mg^{2+} affinity, we compared the ^{1}H-^{13}C heteronuclear multiple-quantum coherence (HMQC) spectra of the side-chain methyl groups (*12*) between the wild-type Rac1 and the P29S mutant (Fig. 1D). The methyl groups with marked chemical shift differences were mainly clustered around the switch1 region, suggesting that the conformation of the switch1 region was affected by the P29S mutation (Fig. 1E). To further characterize the conformational differences in the switch1 region, we prepared the T35A mutant of Rac1, considering the previous report that the Mg^{2+} binding is sensitive to the structural alternations at the

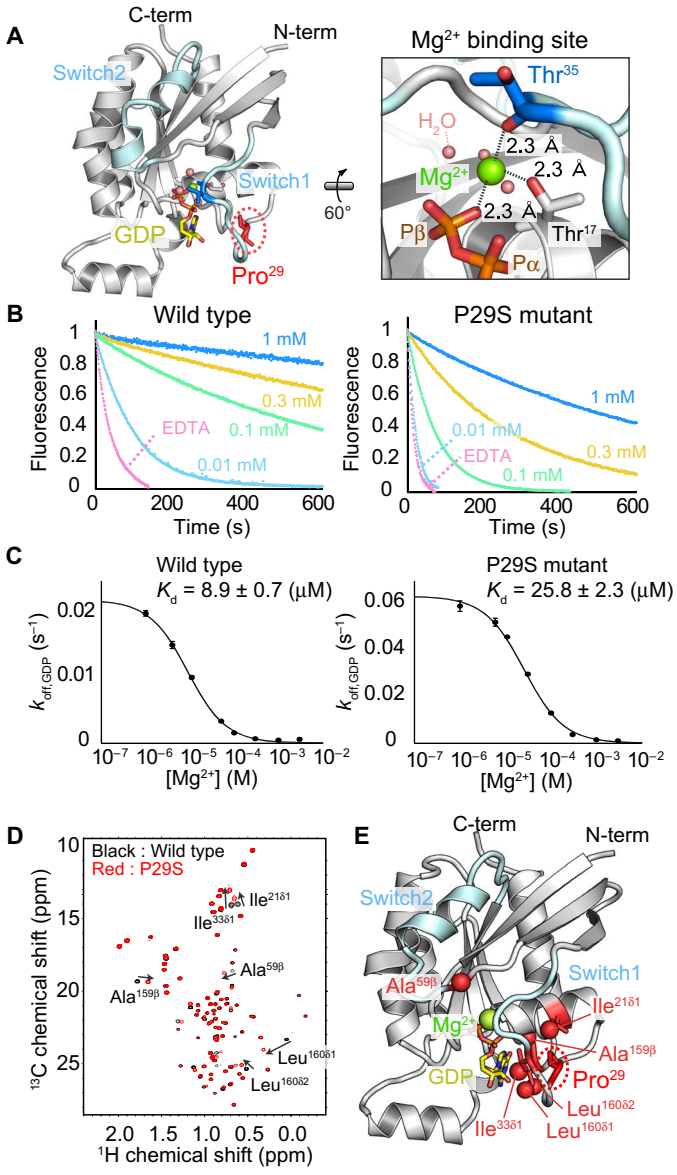

Fig. 1. GDP dissociation rates and NMR spectra of the wild-type Rac1 and the P29S mutant. (**A**) Structure of the Mg^{2+}-binding site. Crystal structure of the GDP-bound Rac2 in the Rac2-Rho GDI complex [Protein Data Bank (PDB) ID: 1DS6] (*8*). The switch regions are colored cyan, and Pro^{29} is colored red. The close-up view of the Mg^{2+}-binding site is shown on the right. (**B**) Mant-GDP dissociation rates of the wild-type Rac1 (left) and the P29S mutant (right) in the presence of various concentrations of Mg^{2+}. The data depicted as EDTA were measured in the presence of 1 mM EDTA. (**C**) Apparent K_d of Mg^{2+} for the wild type (left) and the P29S mutant (right). Each point reflects mean ± SE of three independent experiments. (**D**) Overlay of the ^1H-^{13}C HMQC spectra of the wild type (black) and the P29S mutant (red), measured at 14.1 T (600-MHz ^1H frequency) and 25°C. In the NMR experiments, the R66E background mutation is introduced to suppress the self-association. ppm, parts per million. (**E**) Mapping of the methyl groups with marked chemical shift differences onto the structure of Rac1. The normalized chemical shift differences, Δδ, are calculated by the equation, $\Delta\delta = \{(\Delta\delta_{1H})^2 + (\Delta\delta_{13C}/5.6)^2\}^{0.5}$. The methyl groups with Δδ larger than 0.05 ppm are colored red.

corresponding position in the Ras family (*13*). We found that the T35A mutant shows slower GDP dissociation, as compared to the wild type, and the apparent K_d for Mg^{2+} was calculated to be 5.2 ± 0.8 μM in the mutant, which is slightly stronger than that in the wild type (Fig. 2, A and B, and table S1). Notably, the comparisons of the ^1H-^{13}C HMQC spectra between the wild type and the mutants revealed that the methyl signals from Ala^{42}, which is located in the C-terminal boundary region of switch1, were observed in higher and lower fields in ^1H and ^{13}C dimensions, respectively, as the apparent K_d for Mg^{2+} increases, indicating that the chemical shift values are linearly correlated to the K_d values. The similar chemical shift patterns were observed for the methyl groups located around the switch1 region, strongly suggesting that the conformational changes in the switch1 region are closely related to the differences in the Mg^{2+} affinity (Fig. 2C and fig. S1).

Conformational equilibrium in the switch1 region

Considering the fact that a large portion of the switch1 region was exchange broadened in the ^1H-^{15}N transverse relaxation–optimized spectroscopy (TROSY) spectrum (fig. S2), we hypothesized that the switch1 region exists in a conformational equilibrium on a millisecond-to-microsecond time scale, and changes in the relative population are reflected in the chemical shift differences. To test this hypothesis, we conducted ^{13}C single-quantum (SQ) and ^1H triple-quantum (3Q) Carr-Purcell-Meiboom-Gill (CPMG) relaxation dispersion (RD) experiments to observe the methyl groups (*14*, *15*) and detected significant exchange contributions in the methyl groups surrounding the switch1 region ($Leu^{20\delta1}$, $Ile^{21\delta1}$, $Ile^{33\delta1}$, $Val^{36\gamma1}$, $Val^{36\gamma2}$, $Ala^{42\beta}$, and $Ala^{59\beta}$) (fig. S3). The fitted k_{ex} values were almost the same, around 4000 s^{-1} for all the exchanging methyl groups, indicating that the exchange process can be described by two distinct conformations exchanging in a highly cooperative manner. The major and minor conformations in the wild type are henceforth referred to as states A and B, respectively.

On the basis of the two-state assumption, we simultaneously analyzed the RD curves and exchange-induced changes in the peak positions in the heteronuclear single-quantum coherence (HSQC) and HMQC spectra to describe the cooperative motion (*16*, *17*) and successfully obtained a global k_{ex} value of 4340 ± 140 s^{-1} and a B state population of 0.346 ± 0.007 in the wild type (Fig. 2D and fig. S4). We also performed the same analyses on the mutants and obtained a k_{ex} value of 4680 ± 130 s^{-1} and a B state population of 0.555 ± 0.003 for the P29S mutant and a k_{ex} value of 4030 ± 90 s^{-1} and a B state population of 0.097 ± 0.004 for the T35A mutant. The observed chemical shift differences could be explained well by the changes in the B state population in the mutants, and the B state population correlated well with the apparent K_d for Mg^{2+}, supporting the fact that states A and B represent the high- and low-affinity states for Mg^{2+}, respectively (Fig. 2E). It should be noted that the k_{ex} values are comparable for the wild type and the P29S and T35A mutants, although the populations of the two states are quite different, reflecting that both of the forward and reverse rates of the equilibrium are markedly different between the wild type and the mutants. We also analyzed Rac1 bound to a Rho–GDP dissociation inhibitor (GDI), which stabilizes the Mg^{2+}-bound state and inhibits the GDP dissociation (*8*, *18*). We compared the NMR signals from Ile^{21}, Ile^{33}, and Ala^{42}, which are located over 8 Å distant from Rho-GDI (*8*), to characterize the switch1 conformational states in the Rho-GDI–bound state (Fig.3, A and B). The chemical shifts of the Rho-GDI–bound state were similar to those of the T35A mutant, in which the equilibrium is shifted toward the A state, and actually matched those of the A state of the wild type, calculated from the CPMG RD analyses in the absence of Rho-GDI (Fig. 3, C and D). In addition, we found that the ^{13}C SQ CPMG dispersions of these methyl groups were almost completely suppressed by the binding of Rho-GDI. These

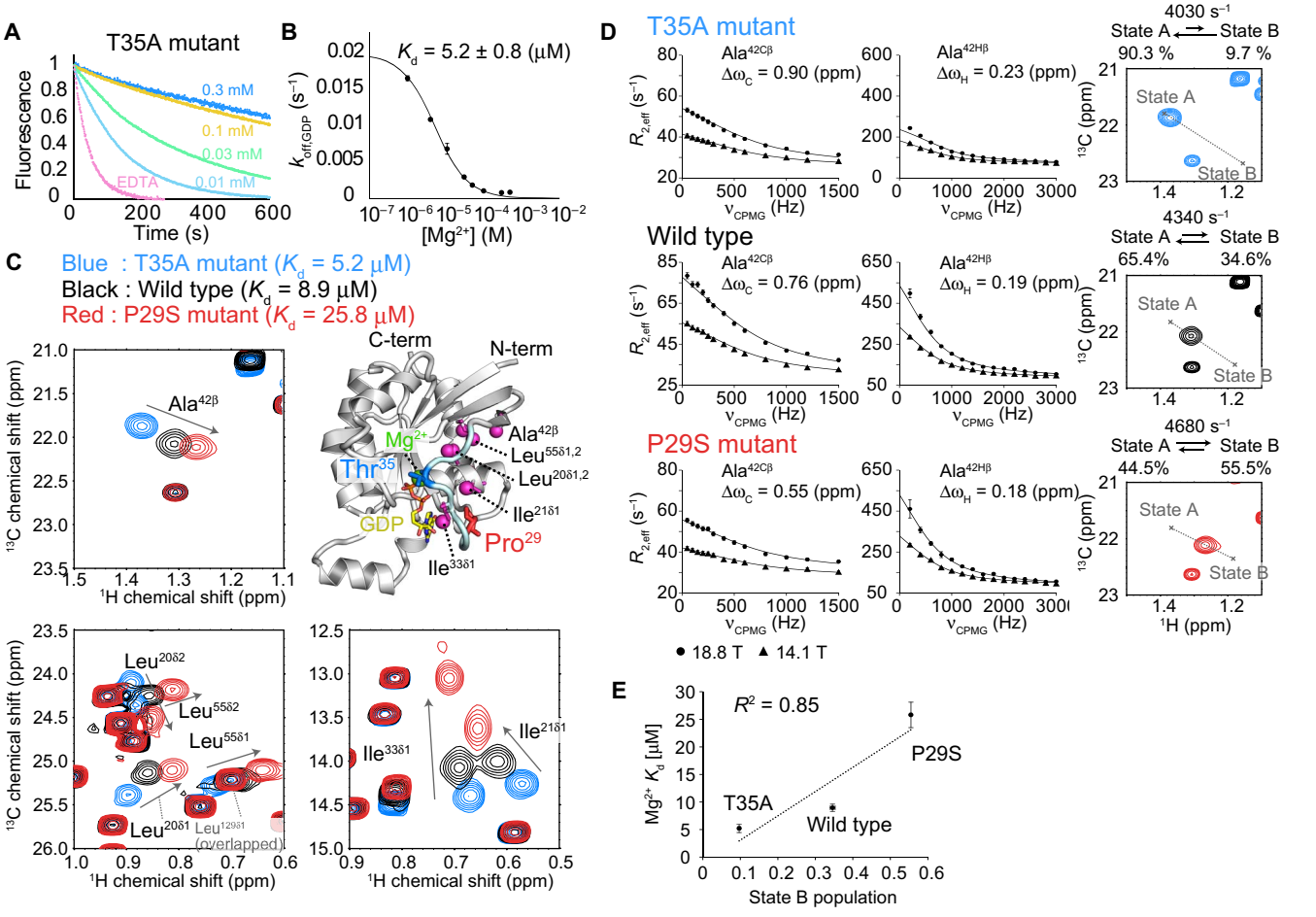

Fig. 2. GDP dissociation in the T35A mutant and conformational exchange processes of Rac1. (**A**) Mant-GDP dissociation rates of the T35A mutant in the presence of various concentrations of Mg^{2+}. The data depicted as EDTA were obtained in the presence of 1 mM EDTA. (**B**) Apparent K_d of Mg^{2+} for the T35A mutant. (**C**) Overlay of the ^1H-^{13}C HMQC spectra of the wild type (black), the P29S mutant (red), and the T35A mutant (blue), measured at 14.1 T (600-MHz ^1H frequency) and 25°C. The methyl groups highlighted in the spectra are mapped onto the structure of Rac1. (**D**) CPMG RD results of the Ala^{42β} methyl groups of the wild type, the P29S mutant, and the T35A mutant. Close-up views of the ^1H-^{13}C HMQC spectra, the chemical shifts of states A and B, and the exchange parameters are also shown. (**E**) Linear correlation plot of the apparent K_d of Mg^{2+} versus the population of the B state. In the NMR experiments, the R66E background mutation is introduced to suppress the self-association.

results demonstrate that the binding of Rho-GDI suppresses the exchange process to trap Rac1 in the A state (Fig. 3E).

Collectively, we concluded that the conformational exchange in Rac1 is characterized well by the global two-state exchange process between the A state with high affinity for Mg^{2+} (K_d on the order of nM or less) and the B state with low affinity for Mg^{2+} (K_d of ~40 μM by extrapolation) and that the crystal structure of Rac1 in the Rho-GDI complex closely corresponds to the structure of the A state. We should also note that the B state population significantly increases in the P29S mutant. These results establish the dynamic mechanism underlying the reduced affinity for Mg^{2+} in the P29S mutant, in which the P29S mutation shifts the preexisting conformational equilibrium to stabilize the Mg^{2+} low-affinity state.

Structure of the low-affinity conformation for Mg^{2+}

To obtain structural insights into the unexplored B state with reduced affinity for Mg^{2+}, we conducted intramolecular paramagnetic relaxation enhancement (PRE) experiments and modeled an atomic structure of the B state using the PREs as distance restraints. We first prepared E31C Rac1 conjugated with (1-oxyl-2,2,5,5-tetramethyl-Δ3-pyrroline-3-methyl)-methanethiosulfonate (MTSL), in which a nitroxide spin label was site-specifically introduced to the switch1 region, and analyzed the intramolecular PREs on the side-chain methyl $^{13}CH_3$, backbone amide NH, and Trp ε-NH protons. Although most of the observed PREs were compatible with the structure of the A state, we found that long-range PREs were observed for the signals located on the C terminus of β2 and the N-terminal half of β3 (residues 45 to 51), which could not be explained from the A state structure (Fig. 4A). A comparison of these PREs with those obtained from the P29S-E31C and E31C-T35A mutants revealed that these long-range PREs became more prominent as the B state population increased, indicating that the proximity between the switch1 and β2-β3 regions is a characteristic feature of the B state structure (Fig. 4B). It should also be noted that complementary PRE patterns were observed for Ala^{13β}, which is expected to become more distant from the switch1 region in the B state under this assumption.

By integrating the PREs from four positions (Glu^{31}, Asp^{63}, Gln^{74}, and Leu^{160}) (fig. S5), we conducted ensemble simulated annealing calculations assuming a two-state ensemble (*19*), in which each ensemble member represents the structure of state A or B. In the calculations, the following assumptions were made: (i) In the ensemble member

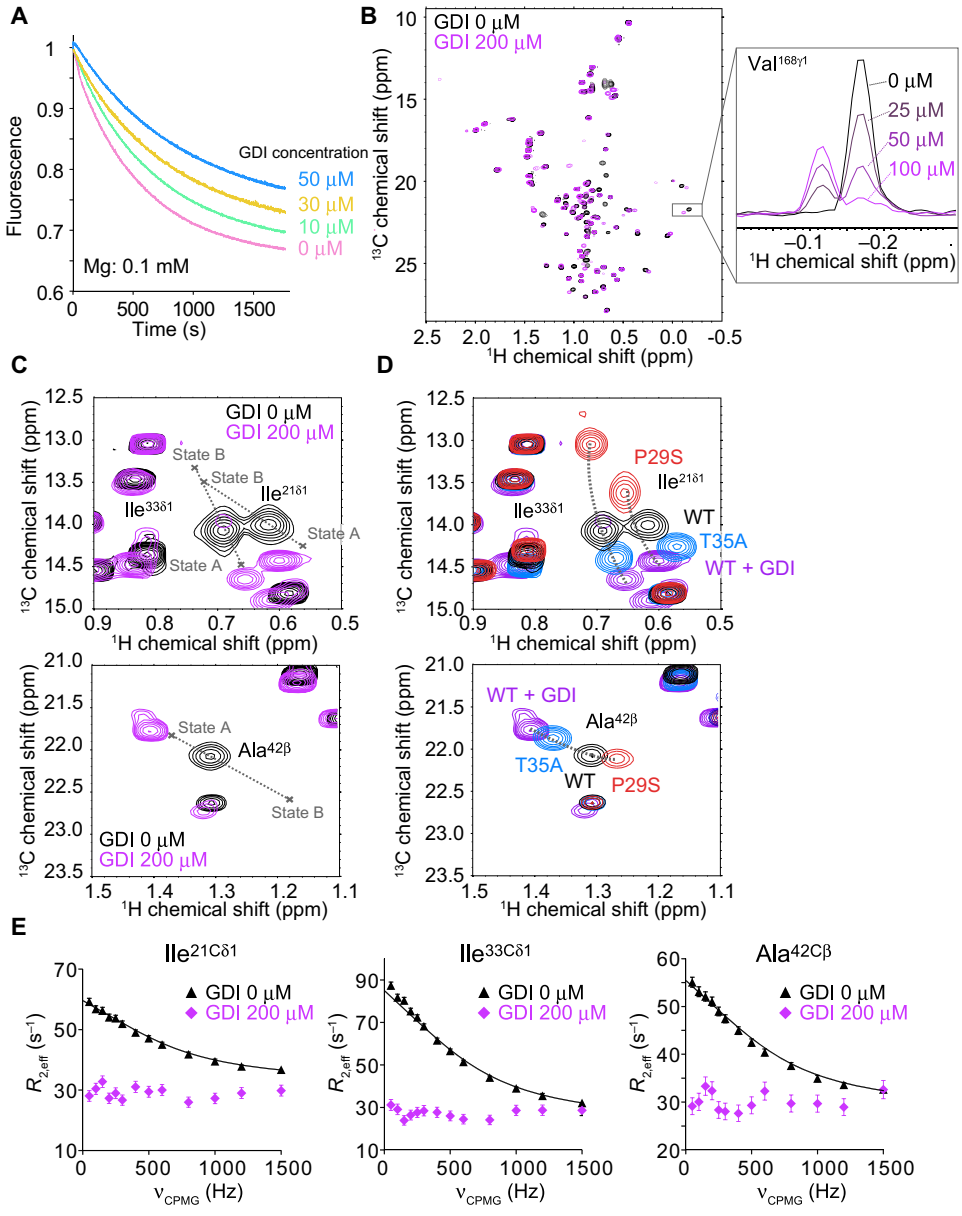

Fig. 3. Mant-GDP dissociation rate measurements and NMR analyses in the presence of Rho-GDI. (**A**) Mant-GDP dissociation rates in the presence of various concentrations of Rho-GDI. Mg^{2+} was added to the final concentration of 0.1 mM. We confirmed that the purified Rho-GDI inhibits GDP dissociation from Rac1. (**B**) Overlay of the ^{1}H-^{13}C HMQC spectra in the absence (black) and presence (purple) of Rho-GDI, measured at 14.1 T (600-MHz ^{1}H frequency) and 25°C. One-dimensional cross sections of the Val$^{168\gamma1}$ signal are shown. The direct interaction was verified from the NMR spectral changes of Rac1 upon the addition of stoichiometric amounts of Rho-GDI. (**C**) Close-up views of the ^{1}H-^{13}C HMQC spectra in the absence (black) and presence (purple) of 200 μM Rho-GDI. Cross marks denote the chemical shifts of states A and B, calculated from the CPMG RD and HSQC/HMQC analyses in the absence of Rho-GDI. (**D**) Overlays of the ^{1}H-^{13}C HMQC spectra of the wild type (WT) in the presence of 200 μM Rho-GDI (purple), the T35A mutant (blue), the wild type in the absence of Rho-GDI (black), and the P29S mutant (red). In the NMR experiments of the wild type in the absence of GDI, the T35A mutant, and the P29S mutant, the R66E background mutation is introduced to suppress the self-association. (**E**) ^{13}C SQ CPMG RD profiles in the absence (black) and presence (purple) of 200 μM Rho-GDI. CPMG RD experiments were performed at 14.1 T (600-MHz ^{1}H frequency) and 25°C.

corresponding to the A state, the atomic coordinates of Rac1 from the crystal structure of the Rho-GDI complex were adopted (*8*). (ii) In the ensemble member corresponding to the B state, the residues around the switch1 region (residues 24 to 47) were allowed to move, and the rest of the residues were held in fixed positions. The validity of the variable region was confirmed on the basis of the analyses of the backbone amide ^{1}H-^{15}N residual dipolar couplings (RDCs), which showed that the RDCs from the region outside switch1 were compatible with those calculated using the Rac1 structure of the Rho-GDI complex (Fig. 5). (iii) The β-sheet structure formed between the β2 and β3 strands was maintained in the B state. This assumption was made because the backbone amide signals from β3 did not exhibit significant chemical shift changes or exchange broadenings. The ensemble weights were set to 0.6 and 0.4 for states A and B, respectively, according to the population obtained from the CPMG RD experiments (fig. S6).

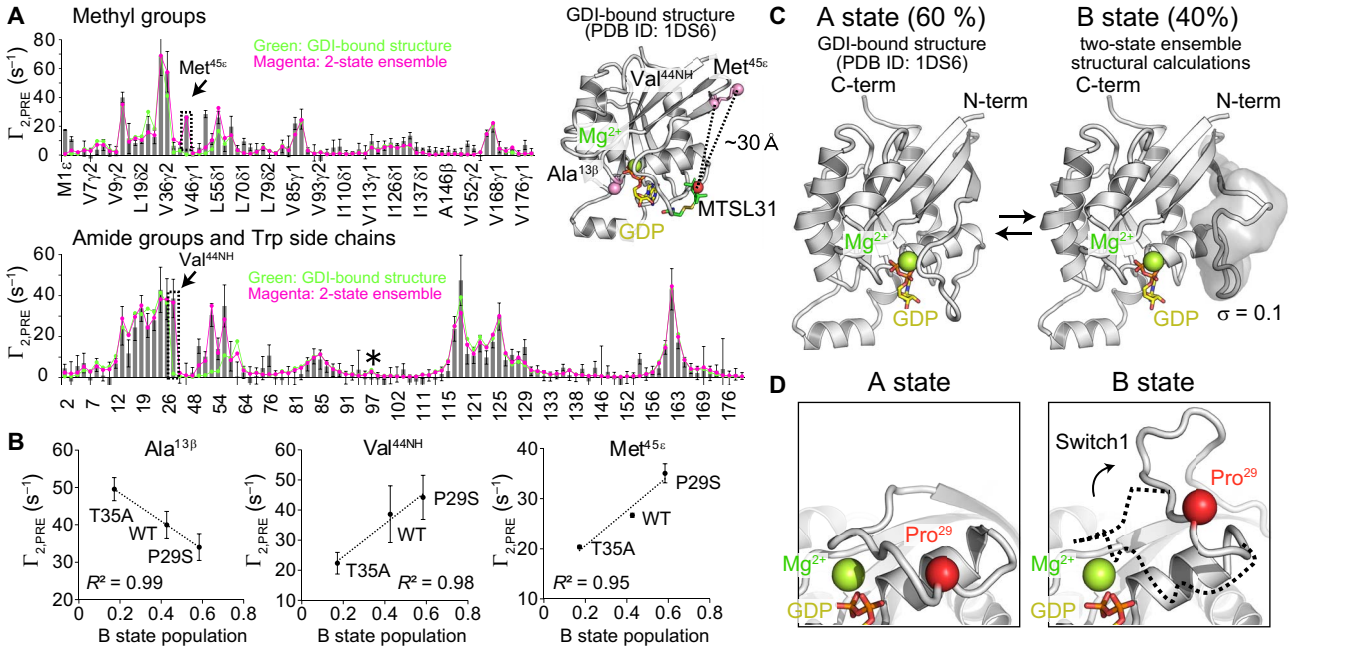

Fig. 4. Intramolecular PRE experiments. (**A**) Plots of intramolecular PREs observed from the MTSL-conjugated E31C. Bar graphs show the experimentally observed PREs, green lines show the back-calculated PREs using the crystal structure of the Rho-GDI complex, and magenta lines show the back-calculated PREs calculated from two-state ensemble structural calculations. Asterisk denotes a Trp side-chain ε-NH signal. Small differences between the observed PREs and the back-calculated PREs were observed in the region around Val^{51}, which is located adjacent to the flexible region (residues 24 to 47) defined in the ensemble calculations. We assume that these differences are attributed to the fact that the side-chain structures are slightly changed from the crystal structure in the B state because these residues are located in the border between the movable and fixed residues. Long-range PREs observed on Val^{44NH} and Met$^{45\varepsilon}$ methyl protons are illustrated on the structure. In the PRE experiments, the R66E background mutation is introduced to suppress the self-association. (**B**) Linear correlation plots of the PREs observed on Ala$^{13\beta}$ methyl, Val^{44NH}, and Met$^{45\varepsilon}$ methyl protons versus the population of the B state estimated under the experimental conditions. Error bars were calculated on the basis of the signal-to-noise ratios of the spectra. (**C**) Structural comparison between the structure of the A state that corresponds to the crystal structure of the Rho-GDI complex and the structure of the B state obtained from the two-state ensemble structural calculations under the PRE-based distance restraints. The structure of the B state represents the lowest-energy structure, and a main-chain atomic probability density map of 20 lowest-energy structures at the contour level of 0.1 is shown as a transparent surface model. (**D**) Close-up views of the switch1 structures of states A and B. The Cα atoms of Pro^{29} are colored red.

On the basis of the ensemble calculations, we successfully constructed an atomic model structure of the B state (Fig. 4C). The *q* factor (*19*) of the PREs from E31C-MTSL decreased from 0.45 to 0.28, and the long-range PREs were well fitted by using a two-state ensemble model (Fig. 4A and fig. S5). In the B state structure, the switch1 region is located distant from the bound GDP and Mg^{2+}, and the carbonyl oxygen of Thr^{35} does not coordinate with the Mg^{2+}, which explains the weaker Mg^{2+} binding affinity in the B state (Fig. 4C and fig. S7A). The structure also suggests that the orientation of the loop forming switch1 is kinked at the position of residue 29 in the B state (Fig. 4D). Because the Pro-to-Ser substitution increases the conformational freedom of the main chain, the P29S mutation will shift the equilibrium to stabilize the B state by favoring the kinked conformation. Although it is difficult to describe the detailed side-chain structures of the B state because of a lack of sufficient structural restraints, the structure shows that the side chains of Thr^{35} and Phe^{37} can become proximate to form an OH-π interaction in the B state, suggesting that the side-chain OH group of Thr^{35} plays important roles in stabilizing the B state structure (fig. S7B). This observation would explain the shift in the equilibrium in the T35A mutant, in which the B state population decreases as compared to the wild type. We expect that the switch1 structure in the B state is inherently flexible and can adopt multiple structures with slightly different loop orientations, because the switch1 structure is not stabilized by interactions with other secondary structural elements. This flexibility likely results in the relatively broad spatial distribution in the calculated structural ensemble of the B state (fig. S7A). The validity of the B state structure was further established from the accelerated molecular dynamics (aMD) simulations (*20*). During the 200-ns aMD trajectory, we could observe the structural transitions accompanying the large structural rearrangements

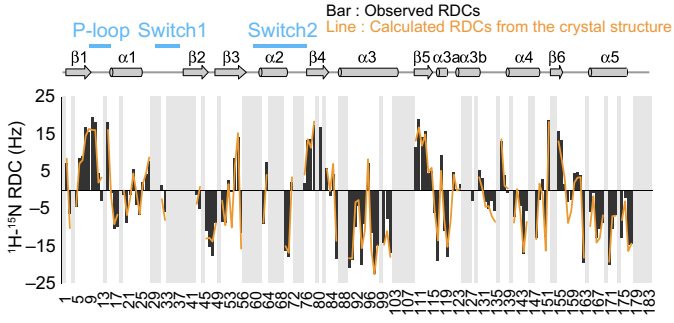

Fig. 5. ^{1}H-^{15}N RDC experiments. Bar graphs represent the experimentally observed RDCs, and orange lines represent the calculated RDCs using the crystal structure of the Rho-GDI complex. The residues with no data are shown with gray backgrounds. In the experiment, the R66E background mutation is introduced to suppress the self-association. The measurements were performed at 14.1 T (600-MHz ^{1}H frequency) and 20°C.

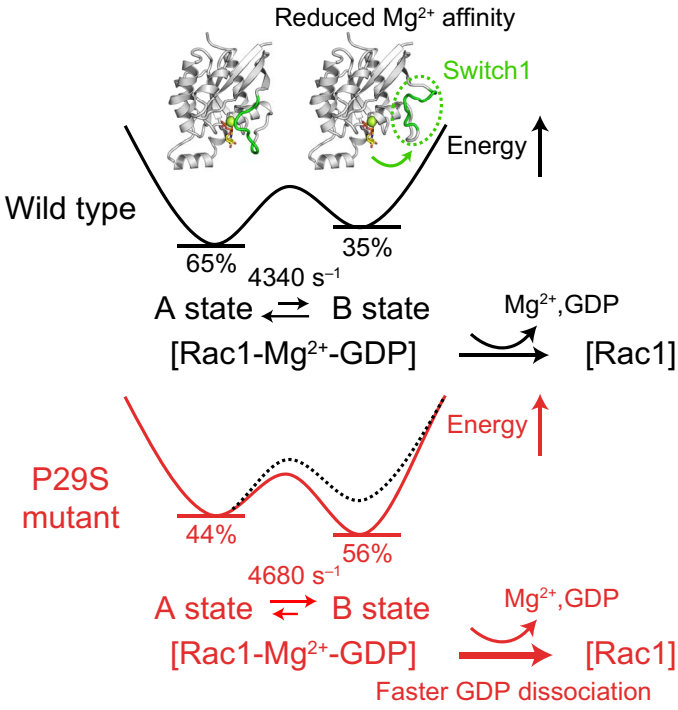

Fig. 6. Conformational landscapes of the wild-type Rac1 and the P29S mutant. The structure of the A state represents the crystal structure of the Rho-GDI complex, and the structure of the B state represents the lowest-energy structure obtained from ensemble structural calculations under the PRE-based distance restraints. The exchange parameters obtained from CPMG RD and HSQC/HMQC analyses are shown.

of the switch1 region, which have similar structural characteristics to those observed in the PRE-based ensemble calculations (fig. S8).

DISCUSSION

On the basis of these results, we revealed that Rac1 in the GDP-bound state exists in a conformational equilibrium between two conformations with different Mg^{2+} affinities, states A and B with high and low affinities for Mg^{2+}, respectively. This equilibrium is shifted toward the B state in the oncogenic P29S mutant, which accelerates GDP dissociation due to its impaired Mg^{2+} coordination. Considering that the A state is the predominant state of the wild-type Rac1 under physiological conditions, it is notable that the introduction of a single-point mutation, P29S, markedly alters the energy landscape to invert the relative populations of the two conformations (Fig. 6). Our results support the proposal that the divergence in a protein's function can be controlled by changing the delicate balance between the states on the energy landscape (*21*), and demonstrate that the conformational landscape alternations can actually occur in vivo, which greatly contributes to the oncogenic activities. The mechanism presented here is totally different from those proposed for the "hotspot" mutants of the Ras family, in which the constitutive activation is caused by the changes in the static structures of the catalytic center for GTP hydrolysis and the guanine nucleotide–binding pocket (*2*, *22*). Furthermore, our mechanism highlights the functional importance of the conformational plasticity of proteins to understand the molecular mechanisms underlying the pathological processes. From a pharmacological point of view, it is worth mentioning that the opening of switch1 in the Mg^{2+} low-affinity state results in the formation of a cryptic drug-binding pocket (*23*). By rationally designing compounds that can bind to the pocket, it would be possible to selectively target the oncogenic P29S mutant and to stabilize the switch1 structure in the B state conformation. In addition, the compounds are expected to exhibit anticancer activities by disrupting the downstream signaling pathways more efficiently in the mutant than in the wild type, because the switch1 region forms the effector-binding surfaces (*1*). Because small G proteins have long been considered to be "undruggable" due to the absence of deep hydrophobic drug-binding pockets on the surface (*24*), our structure paves the way for the development of novel anticancer drugs targeting Rac1.

MATERIALS AND METHODS

Protein expression and purification

The Rac1 protein (human Rac1, residues 1 to 184) was expressed in *Escherichia coli* cells as a glutathione *S*-transferase (GST) fusion protein. Our preliminary analyses revealed that the wild-type protein self-associates into a dimer at concentrations more than 10^2 μM, which is consistent with the previous report (*25*). Therefore, we introduced the R66E mutation to suppress the self-association in all the NMR experiments, except for those related to the Rho-GDI interactions. We confirmed that the introduction of the R66E mutation does not largely affect the apparent K_d for Mg^{2+} and that the chemical shift differences between the wild type and the R66E mutant are observed only for the residues that are in close vicinity to Arg^{66} (fig. S9). The Rac1 mutants were constructed with a QuikChange Site-Directed Mutagenesis Kit (Agilent Technologies). *E. coli* BL21-CodonPlus(DE3)-RP cells (Agilent Technologies), transformed with the pGEX-6P-1 plasmid encoding Rac1, were grown at 37°C in LB media for preparing nonlabeled samples or in deuterated M9 media for preparing isotopically labeled NMR samples. When ^{15}N labeling was required, $^{15}NH_4Cl$ was used as the sole nitrogen source. For the selective $^{13}CH_3$ labeling of methyl groups, [3-^{13}C, 2-^{2}H]-L-alanine (for Alaβ) (200 mg/liter), [methyl-^{13}C, 3,3-$^{2}H_2$]-α-ketobutyric acid (for Ileδ1) (CIL; Cambridge Isotope Laboratories, Inc.) (50 mg/liter), [3-methyl-^{13}C,3,4,4,4-$^{2}H_4$]-α-ketoisovaleric acid (for $Leu^{\delta1}$, $Leu^{\delta2}$, $Val^{\gamma1}$, and $Val^{\gamma2}$) (CIL) (80 mg/liter), [methyl-^{13}C]-L-methionine (for Metε) (CIL) (100 mg/liter), and [2,2,3,3-$^{2}H_4$]-succinic acid (CIL) (2.5 g/liter) were added 1 hour before the induction. The Rac1 protein was induced with 0.1 mM isopropyl β-D-1-thiogalactopyranoside at 20°C for 16 hours and purified as described previously (*5*). Briefly, the protein was purified to homogeneity by chromatography on glutathione Sepharose 4B resin (GE). After cleavage of the GST-tag with PreScission protease (GE), the protein was further purified by size exclusion chromatography using HiLoad 26/60 Superdex 75 pg (GE), in buffer containing 20 mM tris (pH 7.5), 150 mM NaCl, 5 mM $MgCl_2$, and 1 mM dithiothreitol (DTT). To observe the amide signals, the purified protein was incubated at 37°C for 36 hours in $MgCl_2$-free buffer to exchange the amide hydrogen atom from ^{2}H to ^{1}H. NMR samples were prepared by changing the buffer to 20 mM Hepes-NaOH (pH 7.0), 0.5 mM GDP, 5 mM $MgCl_2$, and 5 mM DTT by sequential dilution and concentration with an Amicon Ultra Centrifugal Filter Unit NMWL 10 kDa (Merck Millipore).

The DNA sequence encoding the Rho-GDI protein (human Rho-GDI 1, residues 1 to 204) (*18*), with an N-terminal His^{10}-tag and an HRV 3C protease recognition site, was inserted into the pET24d(+) plasmid (Novagen). The Rho-GDI protein was expressed in *E. coli* BL21-CodonPlus(DE3)-RP cells (Agilent Technologies) and purified

to homogeneity by chromatography on HIS-Select resin (Sigma-Aldrich). After cleavage of the His^{10}-tag with HRV 3C protease (Novagen), the protein was further purified by size exclusion chromatography using HiLoad 26/60 Superdex 75 pg (GE).

Mant-GDP dissociation rate measurements

The dissociation rate of mant-GDP was measured by monitoring the reduction in the fluorescence intensity due to the dissociation of mant-GDP preloaded in Rac1 (*10*). The purified Rac1 protein (20 μM) was incubated at 30°C for 30 min in buffer containing 50 mM tris-HCl (pH 7.5), 100 mM NaCl, 0.1 mM $MgCl_2$, 1 mM DTT, and 50 μM mant-GDP (Invitrogen). The dissociation reaction was initiated by a 100-fold dilution in buffer containing 200 μM GTP and various concentrations of $MgCl_2$. The excitation and emission wavelengths were set to 355 and 448 nm, respectively, with slit widths of 5 nm. The measurements were performed at 30°C.

To estimate the apparent K_d for Mg^{2+} in states A and B, we assumed that the on-rates of Mg^{2+} ($k_{on,Mg2+}$) were not significantly different between the two states and that the differences in the off-rates of Mg^{2+} ($k_{off,Mg2+}$) were mainly responsible for the differences in the apparent K_d for Mg^{2+}. We also assumed that the exchange rate between the two states was far faster than the $k_{off,Mg2+}$. With these assumptions, the experimentally observed K_d ($K_{d,obs}$) can be represented as the weighted average of the apparent K_d values for Mg^{2+} in states A and B ($K_{d,Mg2+,A}$ and $K_{d,Mg2+,B}$) (Eq. 1). To determine the $K_{d,Mg2+,A}$ and $K_{d,Mg2+,B}$ by extrapolation, we used the $K_{d,obs}$ values of the wild type, the P29S mutant, and the T35A mutant of Rac1 and the populations of states A and B (p_A and p_B) obtained from the NMR experiments

$$K_{d,obs} = \frac{p_A k_{off,Mg2+,A} + p_B k_{off,Mg2+,B}}{k_{on,Mg2+}} = p_A K_{d,Mg2+,A} + p_B K_{d,Mg2+,B}$$
$$p_A = 1 - p_B \quad (1)$$

NMR analyses

All experiments were performed on Bruker Avance 500, 600, or 800 spectrometers equipped with cryogenic probes. All spectra were processed by the Bruker TopSpin 2.1 or 3.1 software, and the data were analyzed using Sparky (T. D. Goddard and D. G. Kneller, Sparky 3, University of California, San Francisco, CA). Backbone resonance assignments were obtained from a set of standard triple-resonance experiments, with reference to the previous report (*25*). Resonance assignments of the side-chain methyl signals were obtained by combining out-and-back type triple-resonance experiments (*26*), nuclear Overhauser effect (NOE) analyses based on the crystal structure (PDB ID: 1MH1) (*7*), and mutagenesis approaches. We constructed 16 mutants (M1V, V7I, V8I, V14I, L20I, I21V, I33V, V36I, V44I, M45V, L55I, A59V, L67I, L70I, V77I, and V182M) and compared the ^1H-^{13}C HMQC spectrum of each mutant to that of the wild type.

CPMG RD experiments

The ^{13}C SQ and ^1H 3Q CPMG RD experiments were recorded at 25°C with Bruker Avance 600 and 800 spectrometers (*14*, *15*). The constant-time CPMG relaxation period T was set to 20 ms for ^{13}C SQ and 5 ms for ^1H 3Q experiments. The ν_{CPMG} values were varied between 50 and 1500 Hz for ^{13}C SQ and between 200 and 3000 Hz for ^1H 3Q RD experiments. The values of the effective relaxation rates measured in the presence of a ν_{CPMG} Hz CPMG pulse train, $R_{2,eff}(\nu_{CPMG})$, were calculated using Eq. 2, where $I(\nu_{CPMG})$ and $I(0)$ represent the peak intensities with and without the relaxation period T, respectively.

$$R_{2,eff}(\nu_{CPMG}) = -\frac{1}{T}\ln\left\{\frac{I(\nu_{CPMG})}{I(0)}\right\} \quad (2)$$

The uncertainties of $R_{2,eff}(\nu_{CPMG})$ [$\sigma_{R2,eff}(\nu_{CPMG})$] were calculated using Eq. 3, where $\Delta(\nu_{CPMG})$ represents the signal-to-noise ratio of $I(\nu_{CPMG})$. In cases where $\sigma_{R2,eff}(\nu_{CPMG})$ values were less than 2% of $R_{2,eff}(\nu_{CPMG})$, a minimum value of 2% was used.

$$\sigma_{R_{2,eff}}(\nu_{CPMG}) = \frac{1}{T}\cdot\frac{1}{\Delta(\nu_{CPMG})} \quad (3)$$

Preliminary analyses of the RD curves indicated that the exchange processes are in the fast exchange regime. Thus, for residue-specific fitting, the ^{13}C SQ and ^1H 3Q RD curves obtained with two static magnetic fields were simultaneously fitted to the Luz-Meiboom equation (Eq. 4) (*27*), where Φ_X ($X = {}^{13}C$ or ^1H) denotes the dispersion amplitude parameter, $R_{2,0}$ denotes the intrinsic transverse relaxation rate, k_{ex} denotes the exchange rate, $\Delta\omega_X$ ($X = {}^{13}C$ or ^1H) denotes the chemical shift difference, and p_B denotes the B state population. Although the difference in the relaxation rates of in-phase and antiphase magnetization can result in some errors in the ^1H 3Q CPMG experiments (*15*), we can estimate these errors to be smaller than 0.5 s^{-1} and hence safely ignore these errors in our experimental conditions.

$$R_{2,eff} = R_{2,0} + \frac{\Phi_X}{k_{ex}}\left(1 - \frac{4\nu_{CPMG}}{k_{ex}}\tanh\left(\frac{k_{ex}}{4\nu_{CPMG}}\right)\right)$$
$$\Phi_C = p_B(1-p_B)\Delta\omega_C^2$$
$$\Phi_H = p_B(1-p_B)(3\Delta\omega_H)^2 \quad (4)$$

In the global fitting procedure, the data from $Leu^{20\delta1}$, $Ile^{21\delta1}$, and $Ala^{42\beta}$ were used, because these methyl groups exhibited significant exchange contributions in both the ^1H and ^{13}C dimensions, and their HSQC/HMQC line shapes were expected to be strongly affected by the differences in p_B. The optimization procedure was performed with the in-house–developed program written in the programming language Python 2.7 supplemented with the extension modules NumPy 1.7 and SciPy 0.11.0. The exchange parameters were extracted by minimizing the χ^2 function (Eq. 5), where σ represents the error in the experimental measurement (Eq. 3), $S_X(\nu)$ (X = HSQC or HMQC) denotes the normalized signal intensity at the ^{13}C frequency of ν, and Sc denotes the scaling factor ensuring that the contributions from the first and second terms have roughly the same magnitude. Taking into account that $S_x(\nu)$ values were on the order of 10^3 to 10^5 and a total of 64 points were calculated in the HSQC and HMQC simulations, the Sc value was set to 5.2×10^{-8} in all the calculations. We confirmed that the fitted results were not largely affected when we used the larger or smaller Sc values (3.1×10^{-8} or 1.6×10^{-7}) in the calculations.

$$\chi^2 = \sum\frac{\left(R_{2,eff}^{exp} - R_{2,eff}^{calc}\right)^2}{\left(\sigma_{R_{2,eff}}\right)^2} + Sc\sum\left(S_X(\nu)^{exp} - S_X(\nu)^{calc}\right)^2 \quad (5)$$

We calculated the theoretical values for $R_{2,\mathrm{eff}}$ using the Carver-Richard formula (Eq. 6) (*28*), where Δω represents the SQ ^{13}C chemical shift difference, $\Delta\omega_C$, in the ^{13}C SQ CPMG RD analyses, and the 3Q ^{1}H chemical shift difference, $3\Delta\omega_H$, in the ^{1}H 3Q CPMG RD analyses.

$$R_{2,\mathrm{eff}} = R_{2,0} + \frac{k_{\mathrm{ex}}}{2} - \nu_{\mathrm{CPMG}}\cosh^{-1}[D_+\cosh(\eta_+) - D_-\cos(\eta_-)]$$

$$\eta_\pm = \frac{1}{2\sqrt{2}\nu_{\mathrm{CPMG}}}\left[\pm\Psi + (\Psi^2 + \xi^2)^{1/2}\right]^{1/2}$$

$$D_\pm = \frac{1}{2}\left[\pm 1 + \frac{\Psi + 2\Delta\omega^2}{(\Psi^2 + \xi^2)^{1/2}}\right]$$

$$\Psi = k_{\mathrm{ex}}^2 - \Delta\omega^2$$

$$\xi = -2\Delta\omega k_{\mathrm{ex}}(1 - 2p_B) \quad (6)$$

We calculated the theoretical values for $S_X(\nu)$ by simulating the HSQC and HMQC line shapes in the indirect dimension, which were generated by the Fourier transformation of the evolutions of the SQ and MQ magnetizations [$M_{SQ}(t)$ and $M_{MQ}(t)$], calculated using the modified Bloch-McConnell equation (Eq. 7). In the Fourier transformations, the maximum t_1 values were set in a range from 130 to 400 ms, depending on the signals, and 64 points were calculated. We hypothesized that the intrinsic relaxation rates of the SQ and MQ coherences were the same for simplicity, because the linewidths were largely determined by the exchange broadening effects, and the differences between the SQ and MQ intrinsic relaxation rates were expected to be very small (<2 Hz) in Rac1 (*29*).

$$M_{SQ}(t) = \exp(L_{SQ}t)M_{SQ}(0)$$

$$M_{MQ}(t) = 0.5\left[\exp\left(L_{DQ}\frac{t}{2}\right)\exp\left(L_{ZQ}\frac{t}{2}\right) + \exp\left(L_{ZQ}\frac{t}{2}\right)\exp\left(L_{DQ}\frac{t}{2}\right)\right]M_{MQ}(0)$$

$$M_{SQ}(0) = M_{MQ}(0) = \begin{bmatrix} p_A \\ p_B \end{bmatrix} = \begin{bmatrix} \dfrac{k_{BA}}{k_{AB} + k_{BA}} \\ \dfrac{k_{AB}}{k_{AB} + k_{BA}} \end{bmatrix}$$

$$L_{SQ} = \begin{bmatrix} -k_{AB} - R_{2,0} & k_{BA} \\ k_{AB} & i\Delta\omega_C - k_{BA} - R_{2,0} \end{bmatrix}$$

$$L_{DQ} = \begin{bmatrix} -k_{AB} - R_{2,0} & k_{BA} \\ k_{AB} & i(\Delta\omega_C + \Delta\omega_H) - k_{BA} - R_{2,0} \end{bmatrix}$$

$$L_{ZQ} = \begin{bmatrix} -k_{AB} - R_{2,0} & k_{BA} \\ k_{AB} & i(\Delta\omega_C - \Delta\omega_H) - k_{BA} - R_{2,0} \end{bmatrix} \quad (7)$$

Uncertainties of the parameters were estimated using a bootstrap procedure, where a group of 100 datasets was generated from randomly selected values from the dispersion curves and the HSQC/HMQC peak intensities while maintaining the same total size of the data points.

PRE analyses

For PRE measurements, we prepared the Cys-less mutant of Rac1 (C18S, C105S, and C178S), in which the reactive cysteines were substituted with Ser. Using this construct as a template, the E31C, D63C, Q74C, and L160C single-point mutations were separately introduced to collect site-specific PREs. The purified Rac1 mutants were incubated with a fivefold molar excess of MTSL (Toronto Research Chemicals) for paramagnetic experiments, or (1-acetyl-2,2,5,5-tetramethyl-Δ3-pyrroline-3-methyl) methanethiosulfonate (dMTSL; Toronto Research Chemicals) for diamagnetic experiments, in buffer containing 40 to 50 μM Rac1 Cys mutant protein, 20 mM Hepes-NaOH (pH 7.0), and 5 mM $MgCl_2$. After incubation at room temperature for 30 min, the free MTSL and dMTSL were removed by passage through a NAP-5 gel filtration column (GE). NMR samples were prepared by changing the buffer to 20 mM Hepes-NaOH (pH 7.0), 0.5 mM GDP, and 5 mM $MgCl_2$ using an Amicon Ultra Centrifugal Filter Unit NMWL 10 kDa (Merck Millipore). The protein concentration was adjusted to 50 μM to minimize the effects of nonspecific intermolecular interactions. PRE rates ($\Gamma_{2,\mathrm{PRE}}$) were calculated from the difference in the ^{1}H R_2 relaxation rates between the paramagnetic and diamagnetic states, based on the two–time point protocol described previously (*30*). The delay difference was set to 10 ms, and the measurements were performed at 40°C.

Model structure calculations

The structure of the B state was modeled with the Xplor-NIH software, version 2.48 (*19*, *31*). The initial structure was constructed on the basis of the crystal structure of the Rac2-Rho GDI complex (PDB ID: 1DS6) (*8*). First, the Rac1 model structure was constructed with SWISS-MODEL (*32*) using the atomic coordinates of Rac2 in the complex structure, and then Glu^{31}, Asp^{63}, Gln^{74}, and Leu^{160} were substituted with Cys residues conjugated with MTSL using Xplor-NIH. A three-conformer ensemble representation for the Cys-MTSL groups was used to account for their flexibility. Because the exchange process is in the fast exchange limit and the observed PREs represent the population-weighted averages of the PREs from two exchanging states, we conducted ensemble simulated annealing calculations by assuming a two-state ensemble, in which each ensemble member represents the structure of state A or B. In the ensemble member corresponding to the A state, only the side chains of the MTSL-conjugated Cys were allowed to move, and positions of the rest of the residues were fixed. In the ensemble member corresponding to the B state, the residues around the switch1 region (residues 24 to 47) and the side chains of the MTSL-conjugated Cys were allowed to move, and the rest of the residues were held fixed. The ensemble weights were set to 0.6 for the A state and 0.4 for the B state. The total energy function minimized in the structure calculations contained the PRE pseudo-potential, the term for nonbonded interatomic contacts, the covalent geometry terms for bonds, bond angles, and improper dihedral angles, and a statistical potential to restrain dihedral angles. Hydrogen-bonding distance restraints to preserve the integrity of the β2-β3 sheet portion were also included. The side chains of MTSL-conjugated Cys were prevented from clashing with backbone and Cβ, Hβ atoms, but were allowed to overlap with other side chains to account for the mobility of the tags. During the simulated annealing calculations, PRE back calculations were performed using the Solomon-Bloembergen (SB) equation during the high-temperature stage, which was switched to the SB model-free equation during the cooling phase (*19*). The PRE correlation time was set to 14 ns, which was estimated from the rotational correlation time of

Rac1 calculated using the dipolar and chemical shift anisotropy cross-correlated relaxation rates. In total, 200 ensembles were calculated, and the structures were ranked according to the total energy.

RDC measurements

The ^{1}H-^{15}N RDCs were obtained from the difference in the ^{1}H-^{15}N *J*-coupling constants in aligned (pentaethylene glycol monododecyl ether/hexanol) and isotropic media. The *J*-coupling constants were measured from the differences between the TROSY and HSQC peak positions. The measurements were performed at 20°C. The alignment tensors and the calculated RDCs were obtained by singular value decomposition with the DC computation server developed by the Ad Bax group [National Institutes of Health (NIH)] (https://spin.niddk.nih.gov/bax/nmrserver/dc/svd.html) by using the structure of Rac1 modeled from the crystal structure of the Rac2-Rho GDI complex (PDB ID: 1DS6) (*8*).

MD simulations

The all-atom model of Rac1 was constructed with CHARMM-GUI (*33*) on the basis of the crystal structure of the Rac2-Rho GDI complex (PDB ID: 1DS6) (*8*). The Rac2 sequence was converted to that of Rac1, and the structure including the bound GDP and Mg^{2+} was solvated in a periodic water box with a size of 74 Å × 74 Å × 74 Å using TIP3P water molecules. The system was then neutralized with about 150 mM KCl. MD simulations were performed using the NAMD 2.12 software (*34*) and the CHARMM36 parameter set (*35*). A cutoff distance of 12 Å was used for the van der Waals and short-range electrostatic interactions, and the long-range electrostatic interactions were computed with the particle-mesh Ewald method (*36*). Bonds containing hydrogen atoms were restrained with the SHAKE algorithm (*37*). Bonded and short-range electrostatic interactions were computed every 2 fs, and long-range electrostatic interactions were computed every 4 fs. The system was first energy minimized for 500 steps and then equilibrated under isothermal-isobaric (NPT) conditions for 5 ns, at 1 atm and 310 K. The production simulations were performed for 200 ns, at 1 atm and 310 K. In the aMD simulations, a boost potential was applied to all dihedral angles in the system, and another total boost potential was applied to all individual atoms. The input parameters (E_{dihed}, α_{dihed}, E_{total}, and α_{total}) were calculated using Eq. 8, where $V_{dihed,ave}$ and $V_{total,ave}$ represent average dihedral and total potential energies calculated from the 5-ns conventional MD simulation, N_{res} represents the number of residues, and N_{total} represents the total number of atoms in the system (*38*). Sufficient acceleration was achieved with $a_1 = a_2 = 5$ and $b_1 = b_2 = 0.5$. The trajectories were analyzed using the VMD 1.9.3 software (*39*). The reweighted potential of mean force profiles was calculated by the exponential average algorithm using the PyReweighting Python script (*40*).

$$\begin{aligned} E_{dihed} &= V_{dihed,ave} + a_1 \times N_{res} \\ \alpha_{dihed} &= a_2 \times N_{res}/5 \\ E_{total} &= V_{total,ave} + b_1 \times N_{atoms} \\ \alpha_{total} &= b_2 \times N_{atoms} \end{aligned} \quad (8)$$

SUPPLEMENTARY MATERIALS

Supplementary material for this article is available at http://advances.sciencemag.org/cgi/content/full/5/3/eaav8945/DC1

Table S1. MANT-GDP dissociation rates of Rac1.
Fig. S1. ^{1}H-^{13}C HMQC spectra of the wild-type Rac1 and the T35A mutant.
Fig. S2. ^{1}H-^{15}N TROSY spectra of the wild-type Rac1 and the P29S mutant.
Fig. S3. CPMG RD analyses of the wild-type Rac1.
Fig. S4. Summary of the global fitted results of the CPMG RD and HSQC/HMQC analyses.
Fig. S5. Summary of the intramolecular PRE experiments.
Fig. S6. Summary of the global fitted results of the CPMG RD and HSQC/HMQC analyses of the Cys-less mutant of Rac1.
Fig. S7. Comparison between the structures of states A and B obtained from the two-state ensemble structural calculations.
Fig. S8. MD simulations of Rac1.
Fig. S9. Mg^{2+} affinity and NMR spectra of the R66E mutant of Rac1.

REFERENCES AND NOTES

1. Y. Takai, T. Sasaki, T. Matozaki, Small GTP-binding proteins. *Physiol. Rev.* **81**, 153–208 (2001).
2. I. A. Prior, P. D. Lewis, C. Mattos, A comprehensive survey of Ras mutations in cancer. *Cancer Res.* **72**, 2457–2467 (2012).
3. E. Hodis, I. R. Watson, G. V. Kryukov, S. T. Arold, M. Imielinski, J.-P. Theurillat, E. Nickerson, D. Auclair, L. Li, C. Place, D. DiCara, A. H. Ramos, M. S. Lawrence, K. Cibulskis, A. Sivachenko, D. Voet, G. Saksena, N. Stransky, R. C. Onofrio, W. Winckler, K. Ardlie, N. Wagle, J. Wargo, K. Chong, D. L. Morton, K. Stemke-Hale, G. Chen, M. Noble, M. Meyerson, J. E. Ladbury, M. A. Davies, J. E. Gershenwald, S. N. Wagner, D. S. B. Hoon, D. Schadendorf, E. S. Lander, S. B. Gabriel, G. Getz, L. A. Garraway, L. Chin, A landscape of driver mutations in melanoma. *Cell* **150**, 251–263 (2012).
4. M. Krauthammer, Y. Kong, B. H. Ha, P. Evans, A. Bacchiocchi, J. P. McCusker, E. Cheng, M. J. Davis, G. Goh, M. Choi, S. Ariyan, D. Narayan, K. Dutton-Regester, A. Capatana, E. C. Holman, M. Bosenberg, M. Sznol, H. M. Kluger, D. E. Brash, D. F. Stern, M. A. Materin, R. S. Lo, S. Mane, S. Ma, K. K. Kidd, N. K. Hayward, R. P. Lifton, J. Schlessinger, T. J. Boggon, R. Halaban, Exome sequencing identifies recurrent somatic RAC1 mutations in melanoma. *Nat. Genet.* **44**, 1006–1014 (2012).
5. M. Kawazu, T. Ueno, K. Kontani, Y. Ogita, M. Ando, K. Fukumura, A. Yamato, M. Soda, K. Takeuchi, Y. Miki, H. Yamaguchi, T. Yasuda, T. Naoe, Y. Yamashita, T. Katada, Y. L. Choi, H. Mano, Transforming mutations of RAC guanosine triphosphatases in human cancers. *Proc. Natl. Acad. Sci. U.S.A.* **110**, 3029–3034 (2013).
6. H. K. Bid, R. D. Roberts, P. K. Manchanda, P. J. Houghton, RAC1: An emerging therapeutic option for targeting cancer angiogenesis and metastasis. *Mol. Cancer Ther.* **12**, 1925–1934 (2013).
7. M. Hirshberg, R. W. Stockley, G. Dodson, M. R. Webb, The crystal structure of human rac1, a member of the rho-family complexed with a GTP analogue. *Nat. Struct. Biol.* **4**, 147–152 (1997).
8. K. Scheffzek, I. Stephan, O. N. Jensen, D. Illenberger, P. Gierschik, The Rac-RhoGDI complex and the structural basis for the regulation of Rho proteins by RhoGDI. *Nat. Struct. Biol.* **7**, 122–126 (2000).
9. M. J. Davis, B. H. Ha, E. C. Holman, R. Halaban, J. Schlessinger, T. J. Boggon, RAC1P29S is a spontaneously activating cancer-associated GTPase. *Proc. Natl. Acad. Sci. U.S.A.* **110**, 912–917 (2013).
10. B. Zhang, Y. Zhang, Z. Wang, Y. Zheng, The role of Mg^{2+} cofactor in the guanine nucleotide exchange and GTP hydrolysis reactions of Rho family GTP-binding proteins. *J. Biol. Chem.* **275**, 25299–25307 (2000).
11. R. E. London, Methods for measurement of intracellular magnesium:NMR and fluorescence. *Annu. Rev. Physiol.* **53**, 241–258 (1991).
12. V. Tugarinov, P. M. Hwang, J. E. Ollerenshaw, L. E. Kay, Cross-correlated relaxation enhanced ^{1}H–^{13}C NMR spectroscopy of methyl groups in very high molecular weight proteins and protein complexes. *J. Am. Chem. Soc.* **125**, 10420–10428 (2003).
13. M. Spoerner, C. Herrmann, I. R. Vetter, H. R. Kalbitzer, A. Wittinghofer, Dynamic properties of the Ras switch I region and its importance for binding to effectors. *Proc. Natl. Acad. Sci. U.S.A.* **98**, 4944–4949 (2001).
14. P. Lundström, P. Vallurupalli, T. L. Religa, F. W. Dahlquist, L. E. Kay, A single-quantum methyl ^{13}C-relaxation dispersion experiment with improved sensitivity. *J. Biomol. NMR* **38**, 79–88 (2007).
15. T. Yuwen, P. Vallurupalli, L. E. Kay, Enhancing the sensitivity of CPMG relaxation dispersion to conformational exchange processes by multiple-quantum spectroscopy. *Angew. Chem. Int. Ed.* **55**, 11490–11494 (2016).
16. N. R. Skrynnikov, F. W. Dahlquist, L. E. Kay, Reconstructing NMR spectra of "invisible" excited protein states using HSQC and HMQC experiments. *J. Am. Chem. Soc.* **124**, 12352–12360 (2002).
17. P. Vallurupalli, G. Bouvignies, L. E. Kay, Increasing the exchange time-scale that can be probed by CPMG relaxation dispersion NMR. *J. Phys. Chem. B* **115**, 14891–14900 (2011).
18. N. H. Keep, M. Barnes, I. Barsukov, R. Badii, L.-Y. Lian, A. W. Segal, P. C. E. Moody, G. C. K. Roberts, A modulator of rho family G proteins, rhoGDI, binds these G proteins via an immunoglobulin-like domain and a flexible N-terminal arm. *Structure* **5**, 623–633 (1997).

19. J. Iwahara, C. D. Schwieters, G. M. Clore, Ensemble approach for NMR structure refinement against ^{1}H paramagnetic relaxation enhancement data arising from a flexible paramagnetic group attached to a macromolecule. *J. Am. Chem. Soc.* **126**, 5879–5896 (2004).
20. D. Hamelberg, J. Mongan, J. A. McCammon, Accelerated molecular dynamics: A promising and efficient simulation method for biomolecules. *J. Chem. Phys.* **120**, 11919–11929 (2004).
21. G. Bouvignies, P. Vallurupalli, D. F. Hansen, B. E. Correia, O. Lange, A. Bah, R. M. Vernon, F. W. Dahlquist, D. Baker, L. E. Kay, Solution structure of a minor and transiently formed state of a T4 lysozyme mutant. *Nature* **477**, 111–114 (2011).
22. J. C. Hunter, A. Manandhar, M. A. Carrasco, D. Gurbani, S. Gondi, K. D. Westover, Biochemical and structural analysis of common cancer-associated KRAS mutations. *Mol. Cancer Res.* **13**, 1325–1335 (2015).
23. P. Cimermancic, P. Weinkam, T. J. Rettenmaier, L. Bichmann, D. A. Keedy, R. A. Woldeyes, D. Schneidman-Duhovny, O. N. Demerdash, J. C. Mitchell, J. A. Wells, J. S. Fraser, A. Sali, CryptoSite: Expanding the druggable proteome by characterization and prediction of cryptic binding sites. *J. Mol. Biol.* **428**, 709–719 (2016).
24. A. D. Cox, S. W. Fesik, A. C. Kimmelman, J. Luo, C. J. Der, Drugging the undruggable RAS: Mission possible? *Nat. Rev. Drug Discov.* **13**, 828–851 (2014).
25. R. Thapar, C. D. Moore, S. L. Campbell, Backbone ^{1}H, ^{13}C, and ^{15}N resonance assignments for the 21 kDa GTPase Rac1 complexed to GDP and Mg^{2+}. *J. Biomol. NMR* **27**, 87–88 (2003).
26. V. Tugarinov, L. E. Kay, Ile, Leu, and Val methyl assignments of the 723-residue malate synthase G using a new labeling strategy and novel NMR methods. *J. Am. Chem. Soc.* **125**, 13868–13878 (2003).
27. Z. Luz, S. Meiboom, Nuclear magnetic resonance study of the protolysis of trimethylammonium ion in aqueous solution—Order of the reaction with respect to solvent. *J. Chem. Phys.* **39**, 366–370 (1963).
28. J. P. Carver, R. E. Richards, A general two-site solution for the chemical exchange produced dependence of T_2 upon the Carr-Purcell pulse separation. *J. Magn. Reson.* **6**, 89–105 (1972).
29. V. Tugarinov, L. E. Kay, Estimating side-chain order in [U-^{2}H; $^{13}CH_3$]-labeled high molecular weight proteins from analysis of HMQC/HSQC spectra. *J. Phys. Chem. B* **117**, 13–14 (2013).
30. J. Iwahara, C. Tang, G. Marius Clore, Practical aspects of ^{1}H transverse paramagnetic relaxation enhancement measurements on macromolecules. *J. Magn. Reson.* **184**, 185–195 (2007).
31. C. D. Schwieters, J. J. Kuszewski, N. Tjandra, G. M. Clore, The Xplor-NIH NMR molecular structure determination package. *J. Magn. Reson.* **160**, 65–73 (2003).
32. A. Waterhouse, M. Bertoni, S. Bienert, G. Studer, G. Tauriello, R. Gumienny, F. T. Heer, T. A. P. de Beer. C. Rempfer, L. Bordoli, R. Lepore, T. Schwede, SWISS-MODEL: Homology modelling of protein structures and complexes. *Nucleic Acids Res.* **46**, W296–W303 (2018).
33. S. Jo, T. Kim, V. G. Iyer, W. Im, CHARMM-GUI: A web-based graphical user interface for CHARMM. *J. Comput. Chem.* **29**, 1859–1865 (2008).
34. J. C. Phillips, R. Braun, W. Wang, J. Gumbart, E. Tajkhorshid, E. Villa, C. Chipot, R. D. Skeel, L. Kalé, K. Schulten, Scalable molecular dynamics with NAMD. *J. Comput. Chem.* **26**, 1781–1802 (2005).
35. R. B. Best, X. Zhu, J. Shim, P. E. M. Lopes, J. Mittal, M. Feig, A. D. MacKerell Jr., Optimization of the additive CHARMM all-atom protein force field targeting improved sampling of the backbone ϕ, ψ and side-chain χ_1 and χ_2 dihedral angles. *J. Chem. Theory Comput.* **8**, 3257–3273 (2012).
36. U. Essmann, L. Perera, M. L. Berkowitz, T. Darden, H. Lee, L. G. Pedersen, A smooth particle mesh Ewald method. *J. Chem. Phys.* **103**, 8577–8593 (1995).
37. J.-P. Ryckaert, G. Ciccotti, H. J. C. Berendsen, Numerical integration of the Cartesian equations of motion of a system with constraints: Molecular dynamics of *n*-alkanes. *J. Comput. Phys.* **23**, 327–341 (1977).
38. Y. Miao, F. Feixas, C. Eun, J. A. McCammon, Accelerated molecular dynamics simulations of protein folding. *J. Comput. Chem.* **36**, 1536–1549 (2015).
39. W. Humphrey, A. Dalke, K. Schulten, VMD: Visual molecular dynamics. *J. Mol. Graph.* **14**, 33–38 (1996).
40. Y. Miao, W. Sinko, L. Pierce, D. Bucher, R. C. Walker, J. A. McCammon, Improved reweighting of accelerated molecular dynamics simulations for free energy calculation. *J. Chem. Theory Comput.* **10**, 2677–2689 (2014).

Acknowledgments

Funding: This work was supported, in part, by the Japan Agency for Medical Research and Development (AMED) (grant number JP18ae0101046 to I.S.) and the Ministry of Education, Culture, Sports, Science and Technology (MEXT)/Japan Society for the Promotion of Science KAKENHI (grant number JP17H06097 to I.S.). **Author contributions:** Y.T. performed the experiments. Y.T., K.K., T.K., and I.S. designed the study, analyzed the data, and wrote the paper. **Competing interests:** The authors declare that they have no competing interests. **Data and materials availability:** All data needed to evaluate the conclusions in the paper are present in the paper and/or the Supplementary Materials. Additional data related to this paper may be requested from the authors. An ensemble of the 20 lowest-energy structures of the Rac1 B state has been deposited in the PDB with the accession code 6AGP. The backbone and methyl resonance assignments for Rac1 have been deposited in the Biological Magnetic Resonance Bank with the accession number 27577.

Submitted 31 October 2018
Accepted 28 January 2019
Published 13 March 2019
10.1126/sciadv.aav8945

Citation: Y. Toyama, K. Kontani, T. Katada, I. Shimada, Conformational landscape alternations promote oncogenic activities of Ras-related C3 botulinum toxin substrate 1 as revealed by NMR. *Sci. Adv.* **5**, eaav8945 (2019).